

# Privacy-Net: An Adversarial Approach for Identity-Obfuscated Segmentation of Medical Images

Bach Ngoc Kim

École de Technologie Supérieure  
ngoc-bach.kim.1@ens.etsmtl.ca

Pierre-Marc Jodoin

Université de Sherbrooke  
pierre-marc.jodoin@usherbrooke.ca

Jose Dolz

École de Technologie Supérieure  
jose.dolz@etsmtl.ca

Christian Desrosiers

École de Technologie Supérieure  
christian.desrosiers@etsmtl.ca

## Abstract

*This paper presents a client/server privacy-preserving network in the context of multicentric medical image analysis. Our approach is based on adversarial learning which encodes images to obfuscate the patient identity while preserving enough information for a target task. Our novel architecture is composed of three components: 1) an encoder network which removes identity-specific features from input medical images, 2) a discriminator network that attempts to identify the subject from the encoded images, 3) a medical image analysis network which analyzes the content of the encoded images (segmentation in our case). By simultaneously fooling the discriminator and optimizing the medical analysis network, the encoder learns to remove privacy-specific features while keeping those essentials for the target task. Our approach is illustrated on the problem of segmenting brain MRI from the large-scale Parkinson Progression Marker Initiative (PPMI) dataset. Using longitudinal data from PPMI, we show that the discriminator learns to heavily distort input images while allowing for highly accurate segmentation results.*

## 1. Introduction

Machine learning models like deep convolutional neural networks (CNNs) have achieved outstanding performances in complex medical imaging tasks such as segmentation, registration, and disease detection [46, 21]. However, privacy restrictions on medical data including images impede the development of centralized cloud-based image analysis systems, a solution that has its share of benefits: no on-site specialized hardware, immediate trouble shooting or easy software and hardware updates, among others.

While server-to-client encryption can prevent attacks from outside the system, it cannot prevent cybercriminals

within the system from gaining access to private medical data. Another approach to obfuscate the identity of a patient is to anonymize its data. In case of images, this is done by removing the patient-related DICOM tags or by converting it into a tag-free format such as PNG or NIFTI. However, as shown by Kumar et al. [20] and further illustrated in this paper, the raw content of an image can be easily used to recover the identity of a person with up to 97% of accuracy.

A recent solution for decentralized training on multicentric data is federated learning [25]. The idea behind this strategy is to transfer the training gradients of the data instead of the data itself. While such approach is appealing to train a neural network with data hosted in different hospitals, it does not allow the use of a centralized cloud-based model for making predictions at test time without transmitting patient data.

Another solution for privacy protection is homomorphic encryption (HE) [8, 13, 28]. While it ensures absolute data protection, one can also train a neural network with both encrypted and non-encrypted data. Unfortunately, since the HE operations are limited to multiplication and addition, the non-linear operations of a CNN have to be approximated by polynomial functions which makes neural networks prohibitively slow. For example, [28] reports computation times above 30 minutes to process a single  $28 \times 28$  image using an optimized network with only 954 nodes. Thus, homomorphic neural networks so far proposed have been relatively simplistic [11] and it is not clear how state-of-the-art medical image analysis CNNs like U-Net [33] could be implemented in such framework. Furthermore, HE imposes important communication overhead [34] and its use within a distributed learning framework is still cumbersome [11].

In this paper, we propose a client-server system which allows for the analysis of multi-centric medical images while preserving patient identity. On the client side is an encoder that converts patient-specific data into an identity ob-

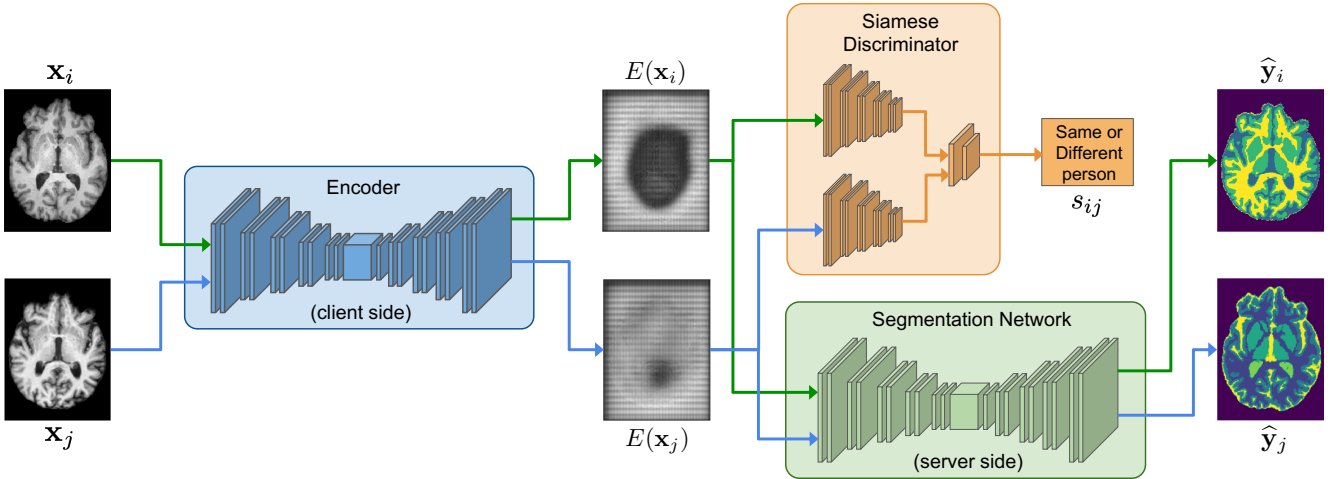


Figure 1. Training configuration of our proposed system: a) a client-side encoder network  $E$  converts input images  $\mathbf{x}_i$  and  $\mathbf{x}_j$  into two feature maps  $E(\mathbf{x}_i)$  and  $E(\mathbf{x}_j)$ , b) the discriminator network  $D$  tries to determine if its input data comes from the same patient ( $s_{ij} = 1$ ) or not ( $s_{ij} = 0$ ), and c) a server-side segmentation network  $S$  segments the encoded images. At test time, the discriminator is removed from the system and images are processed one at a time by the encoder and segmentation network.

fuscated signal containing enough semantic information to analyse its content. The encoded data is then sent to the server where it is analyzed and the results of this analysis are sent back to the client. Since each hospital has the same encoder, the server can keep on updating its system without having access to patient-specific information.

We achieve this with an adversarial learning approach inspired by generative adversarial networks (GAN) [22, 10, 9] but with two main differences. As illustrated in Fig. 1, instead of being a two-network configuration, our system involves three networks: i) an image encoder, ii) a discriminator and iii) a medical image analysis network (a segmentation CNN in our case). Whereas the encoder’s objective is to obfuscate the content of a raw input image, the goal of the discriminator is to determine whether two encoded images come from the same patient or not. The third network is a CNN which analyzes the content of the encoded image. As such, while the encoder tries to fool the discriminator, it must preserve enough information to allow the third network to successfully analyze its content. At test time, the encoder network is deployed on the client side which converts a raw image  $\mathbf{x}$  into an encoded (and yet secure) feature map  $E(\mathbf{x})$ . Thereafter,  $E(\mathbf{x})$  is transferred to the cloud-based server where the segmentation network is deployed. The resulting segmentation map  $\hat{\mathbf{y}}$  is then sent back to the client.

The major contributions of this work are as follows:

- We present the first client-server system for semantic medical image segmentation which allows for identity-preserving distributed learning. Obfuscating identity while preserving task-specific information is particu-

larly challenging for segmentation, which requires to assign a label for each image pixel.

- Our model proposes a novel architecture combining two CNNs for the encoder and segmentation networks with a Siamese CNN for the discriminator. This Siamese discriminator learns identity-discriminative features from image pairs instead of a single image, allowing us to have a variable number of classes (i.e., subject IDs). Unlike the work in [29], our model is trained using both an adversarial Siamese loss and a task-specific loss, thereby providing encoded images that obfuscate identity while preserving the information required for the target task.
- We demonstrate that the privacy-preserving encoder learned with a given dataset can be used to encode images from another dataset, and that these encoded images are useful to update the segmentation network.

## 2. Related Work

**Privacy preserving in visual tasks.** Traditional methods to preserve privacy rely on cryptographic approaches [47, 39] which create local homomorphic encryptions of visual data. Although these methods perform well in some applications, homomorphic cryptosystems typically incur high computational costs [30] and are mostly restricted to simple linear classifiers. This limits their usability in scenarios requiring more complex models like deep neural networks. Another solution consists in extracting feature descriptors from raw images, which are then transferred

to the encrypted dataset server [14]. Nevertheless, sensitive information from original images can be still recovered from standard features, making these systems vulnerable to cyberattacks. An alternative strategy is to employ low-resolution images [5, 4] or image filtering techniques [2, 16] to degrade sensitive information. However, since these approaches also reduce the quality of the visual content, they are limited to a reduced set of tasks such as action or face expression recognition. More recently, McClure et al. [24] proposed using continual learning to circumvent the issue of privacy preservation in the context of multi-center brain tumor segmentation. Nevertheless, unlike our method, their approach is not directly optimized to obfuscate identity from visual data.

**Federated learning.** Federated learning has recently emerged as a solution to build machine learning models based on distributed data sets while preventing data leakage [42, 18, 26, 38, 44]. With this approach, the learning process involves collaboration from all the data owners without exposing their data to others. This can typically be achieved by sharing the architecture and parameters between the client and server during training, along with intermediate representations of the model that may include the gradients, activations and weight updates. Thus, the client downloads the model from the server and updates the weights based on its local data. Yet, a drawback of these strategies is their huge requirements for network bandwidth, memory and computational power, which strongly limits their scalability. More importantly, federated learning does not prevent, at test time, from having to send private data from the client to the server in a scenario such as ours where the server holds the model and processes the data. Also, while HE can be combined to federated learning, its communication protocol is cumbersome and imposes important communication overhead [11, 34].

**Privacy preserving with adversarial learning.** The recent success of adversarial learning has led to the increased adoption of this technique for the protection of sensitive information, particularly in visual data. Xu et al. [43] proposed to add carefully-designed noise to gradients during the learning procedure to train a differentially-private GAN in the context of image recognition. An unsupervised utility loss is employed for training in [32], based on the assumption that removing private characteristics from an image while minimizing changes to the rest of the image yields encoded representations that can be used to learn a target task. However, since the encoding is performed independently of the task, it is potentially sub-optimal for this task. Other works [31, 41, 45, 36] have leveraged adversarial training to jointly optimize privacy and utility objectives. In these works, the mapping functions for the adversarial and task-specific terms are standard classification models where the

number of classes is fixed. In [3], a model which integrates a Variational Autoencoder (VAE) and a GAN is proposed to create an identity-invariant representation of face images. To explicitly control the features to be preserved, they include a discriminator which must predict the identity of the subject in a generated image. As the number of possible labels corresponds to the number of subjects to identify, this approach is not suitable for large-scale applications as the one considered in our work. To alleviate this problem, [29] instead uses a Siamese architecture for the discriminator, which predicts whether two encoded images come from the same subject. In this previous work, an auto-encoder loss is employed as task-agnostic utility objective to avoid the encoder from generating trivial images. In contrast, our privacy-preserving method considers a loss specific to the task of semantic segmentation.

### 3. Methodology

#### 3.1. Proposed system

As shown in Fig. 1, our system implements a zero-sum game involving three separate CNN networks. At the input of our system is a raw image  $\mathbf{x} \in \mathbb{R}^{H \times W \times D}$  (in our case a 3D T1 magnetic resonance image (MRI)). During training, images come in pairs  $(\mathbf{x}_i, \mathbf{x}_j) \in \mathcal{X}^2$ ,  $i \neq j$ . Each image pair is associated to the corresponding ground-truth segmentation maps  $(\mathbf{y}_i, \mathbf{y}_j)$  and binary target  $s_{ij}$  which equals 1 when  $\mathbf{x}_i$  and  $\mathbf{x}_j$  come from the same patient and 0 otherwise. As mentioned in Section 4.1, pairs of images from the same patient are not identical as they were acquired during different acquisition sessions, often months apart.

The first network of our system is an encoder network  $E$  parameterized by  $\theta_E$ . The output of the encoder is a feature map  $E(\mathbf{x}) \in \mathbb{R}^{H \times W \times D}$  which can be seen as an encoded version of the input image. While the encoder could return feature maps of any size, we chose maps with the same size as the input image  $\mathbf{x}$  for three important reasons. First, it allows preserving the information and spatial resolution of the input image. In contrast, using a compressed representation could lead to loss of details. This is why state-of-art segmentation networks employ skip connections that concatenate detailed features from downsampling layers with low-resolution features from upsampling layers [6, 33]. Second, despite the high spatial resolution of encoding  $E(\mathbf{x})$ , it is still more compact than convolutional features of standard networks like VGG which have a lower spatial resolution but a larger number of channels (e.g.,  $14 \times 14 \times 512 = 100,352$  features at the last convolutional layer of VGG compared to  $224 \times 224 \times 1 = 50,176$  features for our encoding, in the case of  $224 \times 224$  images). Third, it enables a fair comparison of segmentation performance with the model using non-encoded images. While training the system, the encoder is fed with a pair of images

$(\mathbf{x}_i, \mathbf{x}_j)$  and returns two encoded images  $E(\mathbf{x}_i)$  and  $E(\mathbf{x}_j)$ . Here,  $\mathbf{x}_i$  and  $\mathbf{x}_j$  are processed individually and not concatenated together.

The second network is the Siamese discriminator network  $D$  with parameters  $\theta_D$ , which is fed with a pair of encoded images. The goal of this network is to determine whether the two images come from the same patient or not. By fooling  $D$  (i.e., maximizing its loss), the encoder provides transformed images that makes difficult identifying the patient. Last, the third CNN is the segmentation network  $S$  with parameters  $\theta_S$ , whose goal is to recover the correct segmentation map  $\mathbf{y}$  given the encoded image  $E(\mathbf{x})$ . During training, both  $E(\mathbf{x}_i)$  and  $E(\mathbf{x}_j)$  are segmented. For this network, we used the widely-adopted U-Net [33], which is very effective at segmenting medical images.

### 3.2. Training losses

As in most adversarial models, our system is trained with two losses that steers the model in opposite directions. In our case, the training procedure involves a segmentation loss and an adversarial discriminator loss:

$$\begin{aligned} \min_{\theta_E, \theta_S} \max_{\theta_D} \mathcal{L}(\theta_E, \theta_S, \theta_D) &= \mathbb{E}_{\mathbf{x}, \mathbf{y} \sim \mathcal{X}, \mathcal{Y}} [\mathcal{L}_{\text{seg}}(S(E(\mathbf{x})), \mathbf{y})] \\ &\quad - \lambda \mathbb{E}_{\mathbf{x}_i, \mathbf{x}_j \sim \mathcal{X}^2} [\mathcal{L}_{\text{dis}}(E(\mathbf{x}_i), E(\mathbf{x}_j), s_{ij})] \end{aligned} \quad (1)$$

where  $\mathcal{L}_{\text{seg}}$  is attached to the segmentation network,  $\mathcal{L}_{\text{dis}}$  is attached to the discriminator, and  $s_{ij} = \mathbb{1}(\text{id}(\mathbf{x}_i) = \text{id}(\mathbf{x}_j))$  is a binary indicator function indicating whether two encoded images come from the same patient or not.

Using  $\hat{\mathbf{y}} = S(E(\mathbf{x}))$  as shorthand notation for the predicted segmentation map, we employ the generalized Dice loss [37] to train the segmentation network, i.e.

$$\mathcal{L}_{\text{seg}}(\hat{\mathbf{y}}, \mathbf{y}) = 1 - \frac{2 \sum_p y_p \hat{y}_p}{\sum_p y_p + \sum_p \hat{y}_p}. \quad (2)$$

For the adversarial loss, we want the discriminator to differentiate subject identity in pairs of encoded images  $E(\mathbf{x}_i)$ ,  $E(\mathbf{x}_j)$ . Here, we define discriminator's classification loss  $\mathcal{L}_{\text{dis}}$  using binary cross entropy:

$$\mathcal{L}_{\text{dis}}(\hat{s}, s) = -s \log \hat{s} - (1 - s) \log(1 - \hat{s}). \quad (3)$$

Like most adversarial models, the parameters of our system cannot be updated all at once through a gradient step. Instead, we first update the encoder and segmentation parameters  $\theta_D, \theta_E$  by taking the following gradient descent step:

$$(\theta_S^{t+1}, \theta_E^{t+1}) \leftarrow (\theta_S^t, \theta_E^t) - \eta \nabla \tilde{\mathcal{L}}(\theta_E^t, \theta_S^t). \quad (4)$$

The gradient is estimated using random batches of image

---

#### Algorithm 1: Privacy-preserving network learning

---

**Input:** Images  $\mathcal{X}$  and ground-truth masks  $\mathcal{Y}$   
**Output:** Network parameters  $\theta_E, \theta_D, \theta_S$

```

/* Initialization */
Initialize network parameters  $\theta_E, \theta_D, \theta_S$ ;
```

```

/* Main loop */
for epoch = 1, ...,  $E_{\text{max}}$  do
    for iter = 1, ...,  $T_{\text{max}}$  do
        Randomly select batch  $\mathcal{B} \subset |\mathcal{X}| \times |\mathcal{X}|$ ;
        Update encoder and segmentation network
        parameters  $(\theta_S, \theta_E)$  using Eq. (4) and (5);
        Update discriminator parameters  $(\theta_D)$  using
        Eq. (6) and (7);
    return  $\theta_E, \theta_D, \theta_S$ ;
```

---

pairs  $\mathcal{B} \subset |\mathcal{X}| \times |\mathcal{X}|$ , as follows:

$$\begin{aligned} \nabla \tilde{\mathcal{L}}(\theta_E, \theta_S) &= \frac{1}{|\mathcal{B}|} \sum_{(i,j) \in \mathcal{B}} \nabla_{\theta_E, \theta_S} \left[ \mathcal{L}_{\text{seg}}(\hat{\mathbf{y}}_i, \mathbf{y}_i) \right. \\ &\quad \left. + \mathcal{L}_{\text{seg}}(\hat{\mathbf{y}}_j, \mathbf{y}_j) - \lambda \mathcal{L}_{\text{dis}}(D(E(\mathbf{x}_i), E(\mathbf{x}_j)), s_{ij}) \right] \end{aligned} \quad (5)$$

We then update the discriminator parameters by taking a gradient ascent step

$$\theta_D^{t+1} \leftarrow \theta_D^t + \eta \nabla \tilde{\mathcal{L}}(\theta_D^t) \quad (6)$$

with the batch gradient computed as

$$\nabla \tilde{\mathcal{L}}(\theta_D) = -\frac{\lambda}{|\mathcal{B}|} \sum_{(i,j) \in \mathcal{B}} \nabla_{\theta_D} \mathcal{L}_{\text{dis}}(D(E(\mathbf{x}_i), E(\mathbf{x}_j)), s_{ij}). \quad (7)$$

Details of our training method are shown in Algo. 1.

### 3.3. Implementation Details

In this study, we used a U-Net architecture [33] but with 3D convolution kernels both for the encoder and the segmentation network. The discriminator is a Siamese network as in [17]. We used a DenseNet architecture [15] with 3D convolution kernels for the CNN backbone. The CNN Siamese backbone (i.e. the left-most CNN inside the Discriminator box in Fig. 1) is used to extract the features of input images. The last layer of the discriminator contains two fully-connected layers to predict if two encoded images are from the same patient. Further details on the networks are reported in the supplementary material.

The system was implemented with Pytorch. We used the Adam optimizer with a learning rate of  $10^{-4}$  for the

	Training	Testing	Total
Nb subjects	269	81	350
Nb images	592	181	773
Nb positive pairs	509	148	657

Table 1. PPMI data used for training and testing our method.

whole training process. The PC used for training is an Intel(R) Core(TM) i7-6700K 4.0GHz CPU, equipped with a NVIDIA GeForce GTX 1080Ti GPU with 12 GB of memory. Training our framework takes roughly 30 minutes per epoch, and around 2 days for the fully-trained system.

Since our networks employ 3D convolutions, and due to the large size of MRI volumes, dense training cannot be applied to the whole volume. Instead, volumes are split into smaller patches of  $64 \times 64 \times 64$ , which allows dense training in our hardware setting. The encoder is initialized with the weights of an auto-encoder, and both the segmentation and discriminator networks were pre-trained on the original images from the the PPMI dataset.

## 4. Experimental results

### 4.1. Datasets

**PPMI.** We experiment on brain tissue segmentation of 5 classes: white matter (WM), gray matter (GM), nuclei, internal cerebrospinal fluid (CSF int.) and external cerebrospinal fluid (CSF ext.). We used the T1 images of the publicly-available Parkinson’s Progression Marker Initiative (PPMI) dataset [23]. We took images from 350 subjects, most of which with a recently diagnosed Parkinson disease. Each subject underwent one or two baseline acquisitions and one or two acquisitions 12 months later for a total of 773 images. PPMI MR images were acquired on Siemens Tim Trio and Siemens Verio 3 Tesla machines from 32 different sites. The images have been registered onto a common MNI space and resized to  $144 \times 192 \times 160$  with a  $1 \text{ mm}^3$  resolution. More information on the MRI acquisition and processing can be found online: [www.ppmi-info.org](http://www.ppmi-info.org).

The dataset was divided into a training and a testing set as shown in Table 1. In order to keep a good balance between the pairs of images, during training and testing, we randomly sampled an equal number of negative and positive samples. Due to the burden of manually annotating volumetric images, we resort to Freesurfer to obtain the segmentation ground-truth, similar to recently-published approaches on large-scale datasets [6, 35].

**MRBrainS.** To further validate the proposed method and investigate its generalization ability, we also tested it on segmenting MRI scans from the MRBrainS 2013 challenge dataset [27]. These images were acquired on a 3.0T Philips Achieva MR scanner and come with expert-annotated seg-

mentation masks including three classes: WM, GM and CSF. We employed a single modality (i.e., MR-T1) in our experiments. Bias correction was performed as a pre-processing step. Original images had a resolution of  $0.96 \times 0.96 \times 3 \text{ mm}^3$  and were registered onto the MNI space using ANTs [1].

### 4.2. Evaluation metrics

To gauge the performance of our system, we use the classification accuracy for measuring the discriminator’s ability to identify images from the same person, and employ the Dice score for evaluating segmentation results. We also use the multiscale structural-similarity (MS-SSIM) score to measure image-to-image distance as a proxy of perceived image quality [40]. Last, to determine if an encoded image can be used to recover the subject in a top- $k$  retrieval setting [19], we use mean average precision (mAP). Considering each encoded test image  $E(\mathbf{x}_i)$  as a separate retrieval task where one must find other encoded images from the same person, the average precision (AP) for  $E(\mathbf{x}_i)$  is given by

$$\text{AP}_i = \frac{1}{\sum_{j \neq i} s_{ij}} \sum_{k=1}^{|\mathcal{X}|} (\text{precision}@k)_i \cdot s_{ik}, \quad (8)$$

where  $\text{precision}@k$  is the precision at cut-off  $k$ , i.e. the ratio of  $k$  encoded images most similar to  $E(\mathbf{x}_i)$  which belong to the same person. mAP is then the mean of AP values computed over all test examples.

## 4.3. Results

### 4.3.1 Results on non-encoded images

At first, we processed the dataset without the adversarial component, i.e, by independently training the segmentation and the discriminator networks without the encoder. We call this setting *non-encoded* in our results. In the first row of Table 2, we see that the discriminator obtains a testing accuracy of 95.3%. This underlines how easy it is for a neural network to recognize a patient based on the content of a brain MRI. More surprising is the 97% classification accuracy that we obtain by simply thresholding the image-to-image MS-SSIM score. This can be explained by the inter- and intra-subject MS-SSIM distribution plots shown in the third row of the first column of Fig. 2. As can be seen, when considering non-encoded images, the intra-subject MS-SSIM scores (red curve) are significantly larger than that of the inter-subjects (blue curve). This again illustrate the ease of recognizing the identity of a person based on the content of a medical image.

The PPMI segmentation Dice scores on non-encoded image for the five regions are in the first row of Table 3. We also report the overall Dice computed as the mean of Dice scores in all regions, weighted by the regions’ size. These

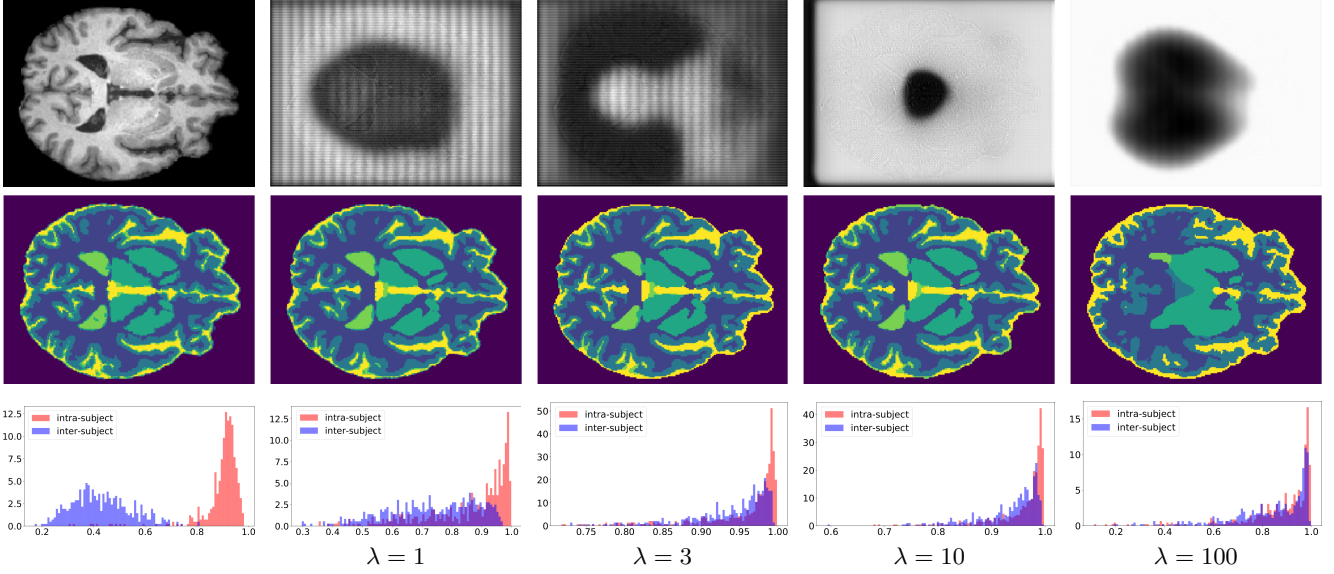


Figure 2. Impact of discriminator loss ( $\lambda$ ). [First column] (Top row): input MRI image  $\mathbf{x}$ , (Second row): ground truth segmentation map  $\mathbf{y}$ , (Third row): distribution of inter- and intra-subject MS-SSIM score on the PPMI dataset. [Remaining columns], (Top row): encoded image  $E(\mathbf{x})$ , (Second row): predicted segmentation  $\hat{\mathbf{y}}$  and (Third row): distribution of MS-SSIM values between encoded images  $E(\mathbf{x}_i)$  and  $E(\mathbf{x}_j)$ .

	Accuracy			mAP
	MS-SSIM	$D_{\text{adv}}$	$D_{\text{new}}$	
Non-encoded	0.970	—	0.953	0.850
Encoded	$\lambda = 1$	0.564	0.520	0.598
	$\lambda = 3$	0.533	0.537	0.615
	$\lambda = 10$	0.510	0.523	0.577
	$\lambda = 100$	0.503	0.516	0.513

Table 2. Same-subject prediction accuracy on test examples obtained by thresholding MS-SSIM scores, using the adversarial discriminator ( $D_{\text{adv}}$ ), or training a separate discriminator on the encoded image ( $D_{\text{new}}$ ). The mAP column is the mean average precision of a top- $k$  retrieval analysis using the Siamese discriminator’s embedding as representation. Results are reported for non-encoded images or encoded images for different  $\lambda$  values.

results correspond roughly to those obtained in recent publications for the same architecture [7]. Note that the nuclei and the internal CSF have a lower Dice due to the smaller size of these regions.

#### 4.3.2 Adversarial results

We report adversarial results obtained with different values of parameter  $\lambda$ , which controls the trade-off between segmentation accuracy and identity obfuscation. The first row of Fig. 2 shows encoded images  $E(\mathbf{x})$  next to the raw input MRI  $\mathbf{x}$ . As can be seen, the larger the  $\lambda$  value is, the more distorted the encoded image gets. Nonetheless, ex-

	GM	WM	Nuclei	CSF int.	CSF ext.	Overall
Non-enc	0.941	0.853	0.657	0.665	0.825	0.848
$\lambda = 1$	0.925	0.824	0.580	0.598	0.752	0.812
$\lambda = 3$	0.899	0.793	0.549	0.550	0.693	0.778
$\lambda = 10$	0.881	0.796	0.555	0.531	0.685	0.771
$\lambda = 100$	0.847	0.692	0.454	0.405	0.513	0.684

Table 3. Segmentation Dice score on the PPMI test set for different values of  $\lambda$ . Non-enc refers to the model trained with non-encoded images.

cept for extreme cases (e.g.,  $\lambda = 100$ ) the encoded images contain enough information for the segmentation network to recover a good segmentation map (c.f., the second row of Fig. 2). The obfuscating power of our method is also illustrated by the MS-SSIM plots (c.f., third row of Fig. 2). As  $\lambda$  increases, the distribution of inter-subject MS-SSIM between encoded images  $E(\mathbf{x}_i)$  and  $E(\mathbf{x}_j)$  becomes more and more similar to that of intra-subjects.

The encoder’s ability to obfuscate identity is evaluated quantitatively in Table 2. Four different techniques are used to measure this property. First, based on the observation that the distribution of MS-SSIM values differs between images from the same patient and images from different patients (c.f., last row of Fig. 2), we compute the accuracy obtained by the best possible thresholding of MS-SSIM values (i.e., values below or equal to the threshold correspond to same patient images, and those above to different patient images). Second, we report the classification accuracy of the discriminator used for training the encoder, denoted as  $D_{\text{adv}}$  in Ta-

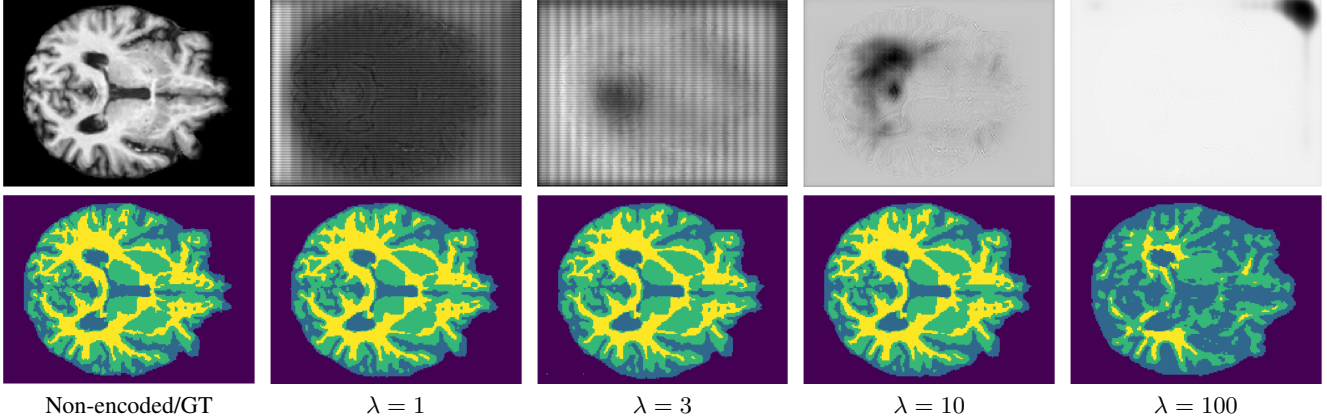


Figure 3. Test results on the MRBrainS dataset. [First column] (Top row): input MRI image  $\mathbf{x}$ , (Bottom row): ground truth segmentation map  $\mathbf{y}$ . [Remaining columns], (Top row): encoded image  $E(\mathbf{x})$ , (Bottom row): predicted segmentation  $\hat{\mathbf{y}}$  with re-trained segmentation networks on MRBrainS

ble 2. Third, since the encoder was trained to fool  $D_{\text{adv}}$ , we also trained a new ResNet discriminator ( $D_{\text{new}}$ ) as in [12] on the fixed encoded images to measure how good the encoder is with respect to an independent network that was not involved in training our system. Last, to assess whether an encoded image can be used to find the corresponding subject with a retrieval method, we considered the embedding of Siamese discriminator  $D_{\text{new}}$  as representation of each encoded test image and used Euclidean distance to find most similar encoded images. We employ mAP to measure retrieval performance.

Results in Table 2 show the same trend for all four obfuscation measures. When images are not encoded, identifying the subject’s identity either by comparing two images or using a retrieval-based approach is fairly easy. However, this becomes much harder for encoded images, with accuracy and mAP rates dropping as  $\lambda$  increases. Moreover, as shown in column  $D_{\text{new}}$ , employing a discriminator trained independently from the encoder does not help re-identify the subject’s ID. This demonstrates the robustness of our method to classification approaches. These results underline the fact that the encoder does not only change image intensity values, but also the structure of the image. Our system thus prevents from recognizing the identity of a patient both when considering an encoded image pair. Furthermore, despite these structural changes, the segmentation network can still recover good segmentation maps, even for  $\lambda=10$  (c.f., Table 3).

#### 4.3.3 Distributed learning

A large dataset such as PPMI with per-patient longitudinal data is required to train end-to-end our system. However, once trained, the encoder is fixed and used as an identity obfuscation module by the clients. On the server side, the segmentation network keeps receiving newly acquired images

		GM	WM	CSF	Overall
No retrain	$\lambda = 1$	0.768	0.822	0.804	0.796
	$\lambda = 3$	0.767	0.852	0.798	0.804
	$\lambda = 10$	0.757	0.798	0.768	0.772
	$\lambda = 100$	0.499	0.464	0.648	0.537
Retrain	$\lambda = 1$	0.819	0.827	0.823	0.821
	$\lambda = 3$	0.794	0.807	0.831	0.814
	$\lambda = 10$	0.780	0.747	0.797	0.790
	$\lambda = 100$	0.605	0.360	0.572	0.586

Table 4. Segmentation Dice score on the MRBrainS dataset for different values of  $\lambda$ . (Top) the CNNs have not been retrained while (Bottom) the segmentation network has been retrained following a distributed learning approach.

and thus can be retrained with it. In order to illustrate this, we used images from the MRBrainS dataset which were acquired with a different acquisition protocol than PPMI and have three labels instead of five, i.e., WM, GM, and CSF.

We first tested on MRBrainS images our model pre-trained with PPMI data. In order to match the three-class ground-truth, we merged the CSF int. and CSF ext. outputs into a single CSF class, and the GM and nuclei outputs into a single GM class. Results for different  $\lambda$  values are shown at the top of Table 4. As expected, these results are slightly worse than those on PPMI (see Table 3). However, as can be seen at the bottom of Table 4, segmentation accuracy improves when the segmentation network is retrained on MRBrainS data following a distributed learning schedule. This shows that the segmentation network of our system can be updated, even after being deployed onto a cloud server. Segmentation maps as well as encoded MRBrainS images are given in Fig 3.

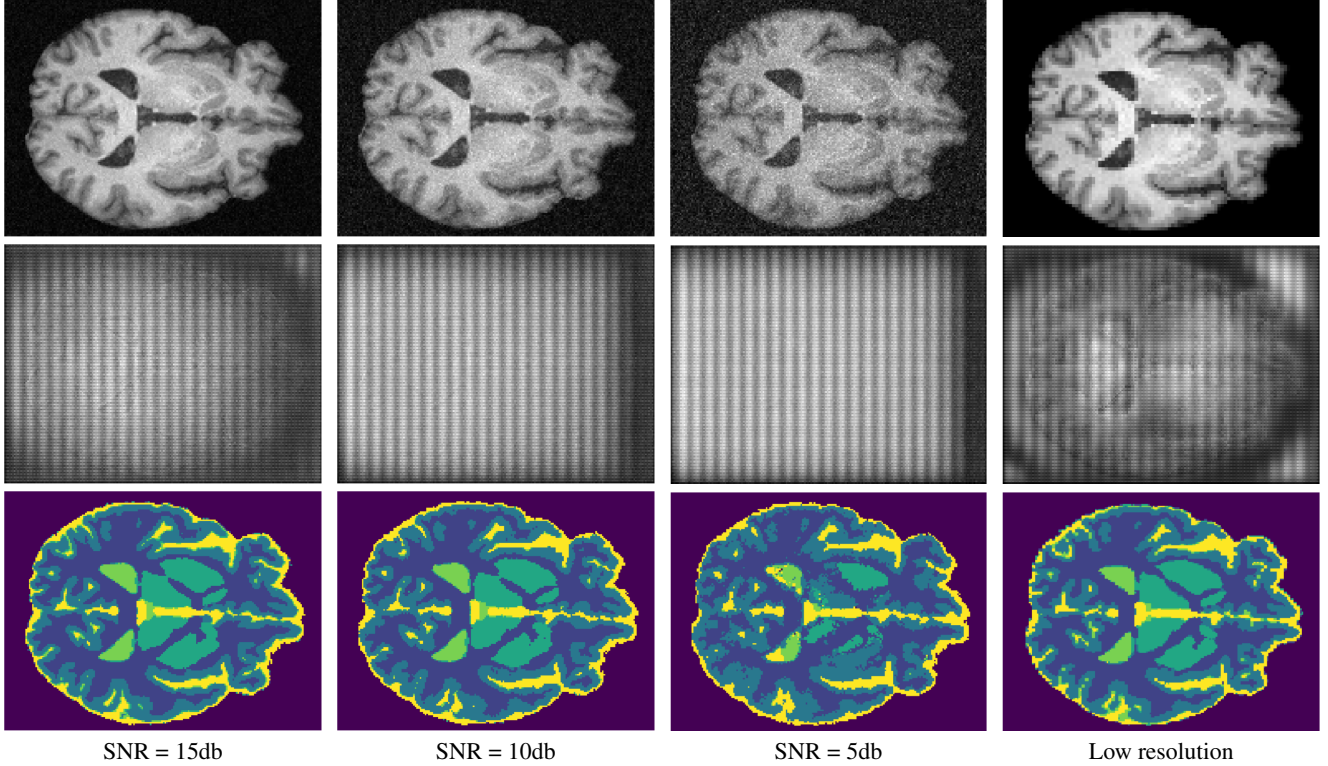


Figure 4. Segmentation with different noise level and a lower resolution setting. (Top row): Degraded images, (Middle row): Encoded images, (Bottom row): Segmentation Results

	GM	WM	Nuclei	CSF int.	CSF ext.	Overall
Noise (15dB)	0.921	0.818	0.572	0.585	0.743	0.808
Noise (10dB)	0.917	0.804	0.566	0.582	0.696	0.797
Noise (5dB)	0.821	0.706	0.514	0.472	0.331	0.669
Low res.	0.881	0.781	0.552	0.516	0.683	0.759

Table 5. Segmentation Dice score on PPMI dataset with different levels of Rician noise (measured in dB) and low resolution setting.

#### 4.3.4 Robustness analysis

To make sure that our system does not work only on high-quality images such as those of PPMI, we performed a robustness analysis where we trained our method on the original PPMI dataset (with  $\lambda = 1$ ) and tested it on noisy versions of the PPMI test images or on images with a lower  $2 \times 2 \times 2 \text{ cm}^3$  resolution. Results are provided in Fig. 4 and Table 5. As can be seen, the encoding and segmentation is not much affected by noise. The segmentation accuracy is close to the one obtained on the original PPMI test set, with overall Dice scores around 80% for noisy images with an SNR of 15db or 10db. Reducing image resolution seems to induce more significant changes in the encoding, however the segmentation network appears robust to these changes.

#### 4.3.5 Runtime

In terms of runtime, an average of 0.08 second is required to encode an image on a NVIDIA GTX 1080Ti, whereas the entire segmentation process requires around 0.1 seconds per image. This runtime is negligible compared to the 8 to 12 hours required by Freesurfer. Training curves illustrating the evolution of different loss terms and performance metrics can be found in the supplementary material.

## 5. Discussion and conclusion

In this work, we presented a novel framework which integrates an encoder, a segmentation CNN and a Siamese network to preserve the privacy of medical imaging data. Experimental results on two independent datasets have shown that the proposed method can preserve the identity of a patient while maintaining the performance on the target task. While this is an interesting application *per se*, it opens the door to appealing potential uses. For example, this approach can be integrated in a continual learning scenario trained on a decentralized dataset, where images have to be shared across institutions but privacy needs to be preserved. From a clinical perspective, obfuscating visual data in addition to current anonymization techniques may foster multi-centre collaborations, resulting in larger datasets as

well as more complete and heterogeneous clinical studies.

Additionally, we have shown that the proposed privacy-preserving model generalizes well to novel datasets, unlike similar works [3] which cannot generalize to encoded images of subjects not seen in training. This facilitates the scalability of our approach to new datasets or tasks. As preliminary step towards preventing privacy leakage in medical imaging data, this study has however some limitations. For example, the domain shift between employed datasets is not significantly large, since both include MRI images of adult brains (even though the acquisition protocols and parameters across scanners differ). Although similar domain shift has resulted in a performance degradation in segmentation networks [6], results demonstrate the good generability of the proposed method in these cases. Future investigations will explore the generalization capabilities of the trained encoder on datasets where the domain shift is larger, for example, between infant and adult brains or even between different image modalities such as MRI and CT.

## Acknowledgements

We acknowledge the support of the Natural Sciences and Engineering Research Council of Canada (NSERC), and thank NVIDIA corporation for supporting this work through their GPU grant program.

## References

- [1] B. Avants, N. Tustison, G. Song, PA Cook, A. Klein, and JC Gee. A reproducible evaluation of ants similarity metric performance in brain image registration. *Neuroimage*, 54(3):2033–2044, 2011. 5
- [2] Daniel J Butler, Justin Huang, Franziska Roesner, and Maya Cakmak. The privacy-utility tradeoff for remotely teleoperated robots. In *Proc of ACM/IEEE ICHRI*, pages 27–34, 2015. 3
- [3] Jiawei Chen, Janusz Konrad, and Prakash Ishwar. Vgan-based image representation learning for privacy-preserving facial expression recognition. In *Proc of CVPR-W*, pages 1570–1579, 2018. 3, 9
- [4] Jiawei Chen, Jonathan Wu, Kristi Richter, Janusz Konrad, and Prakash Ishwar. Estimating head pose orientation using extremely low resolution images. In *proc of IEEE SSIAI*, pages 65–68, 2016. 3
- [5] Ji Dai, Behrouz Saghafi, Jonathan Wu, Janusz Konrad, and Prakash Ishwar. Towards privacy-preserving recognition of human activities. In *proc of ICIP*, pages 4238–4242, 2015. 3
- [6] Jose Dolz, Christian Desrosiers, and Ismail Ben Ayed. 3D fully convolutional networks for subcortical segmentation in MRI: A large-scale study. *NeuroImage*, 170:456–470, 2018. 3, 5, 9
- [7] J. Dolz, K. Gopinath, J. Yuan, H. Lombaert, C. Desrosiers, and I. Ben Ayed. Hyperdense-net: A hyper-densely connected CNN for multi-modal image segmentation. *IEEE TMI*, 38(5):1116–1126, 2019. 6
- [8] N. Dowlin, R. Gilad-Bachrach, K. Laine, K. Lauter, M. Naehrig, and J. Wernsing. A reproducible evaluation of ants similarity metric performance in brain image registration. In *proc of ICML*, 2016. 1
- [9] Yaroslav Ganin, Evgeniya Ustinova, Hana Ajakan, Pascal Germain, Hugo Larochelle, François Laviolette, Mario Marchand, and Victor Lempitsky. Domain-adversarial training of neural networks. *JMLR*, 17(1):2096–2030, 2016. 2
- [10] Ian Goodfellow, Jean Pouget-Abadie, Mehdi Mirza, Bing Xu, David Warde-Farley, Sherjil Ozair, Aaron Courville, and Yoshua Bengio. Generative adversarial nets. In *proc NIPS*, pages 2672–2680, 2014. 2
- [11] Stephen Hardy, Wilko Henecka, Hamish Ivey-Law, Richard Nock, Giorgio Patrini, Guillaume Smith, and Brian Thorne. Private federated learning on vertically partitioned data via entity resolution and additively homomorphic encryption. *ArXiv*, abs/1711.10677, 2017. 1, 3
- [12] Kaiming He, Xiangyu Zhang, Shaoqing Ren, and Jian Sun. Deep residual learning for image recognition. *CoRR*, abs/1512.03385, 2015. 7
- [13] Ehsan Hesamifard, Hassan Takabi, and Mehdi Ghasemi. Cryptodl: Deep neural networks over encrypted data. *CoRR*, abs/1711.05189, 2017. 1
- [14] Chao-Yung Hsu, Chun-Shien Lu, and Soo-Chang Pei. Homomorphic encryption-based secure SIFT for privacy-preserving feature extraction. In *proc of MWSF-III*, volume 7880, 2011. 3
- [15] Gao Huang, Zhuang Liu, and Kilian Q. Weinberger. Densely connected convolutional networks. In *proc CVPR*, 2017. 4
- [16] Ahmad Jalal, Md Zia Uddin, and T-S Kim. Depth video-based human activity recognition system using translation and scaling invariant features for life logging at smart home. *IEEE TCE*, 58(3):863–871, 2012. 3
- [17] Gregory Koch, Richard Zemel, and Ruslan Salakhutdinov. Siamese neural networks for one-shot image recognition. In *proc of ICML*, 2015. 4
- [18] Jakub Konecný, H. Brendan McMahan, Daniel Ramage, and Peter Richtárik. Federated optimization: Distributed machine learning for on-device intelligence. *CoRR*, abs/1610.02527, 2016. 3
- [19] Kuldeep Kumar, Laurent Chauvin, Matthew Toews, Olivier Colliot, and Christian Desrosiers. Multi-modal brain fingerprinting: a manifold approximation based framework. *bioRxiv*, 2017. 5
- [20] K. Kumar, M. Toews, L. Chauvin, O. Colliot, and C. Desrosiers. Multi-modal brain fingerprinting: A manifold approximation based framework. *NeuroImage*, 183:212 – 226, 2018. 1
- [21] Geert Litjens, Thijs Kooi, Babak Ehteshami Bejnordi, Arnaud Arindra Adiyoso Setio, Francesco Ciompi, Mohsen Ghafoorian, Jeroen Awm Van Der Laak, Bram Van Ginneken, and Clara I Sánchez. A survey on deep learning in medical image analysis. *Media*, 42:60–88, 2017. 1
- [22] Pauline Luc, Camille Couprie, Soumith Chintala, and Jakob Verbeek. Semantic segmentation using adversarial networks. *CoRR*, abs/1611.08408, 2016. 2

[23] Kenneth Marek, Danna Jennings, Shirley Lasch, Andrew Siderowf, Caroline Tanner, Tanya Simuni, Chris Coffey, Karl Kieburtz, Emily Flagg, Sohini Chowdhury, et al. The parkinson progression marker initiative (ppmi). *Progress in neurobiology*, 95(4):629–635, 2011. 5

[24] Patrick McClure, Charles Y Zheng, Jakub Kaczmarzyk, John Rogers-Lee, Satra Ghosh, Dylan Nielson, Peter A Bandettini, and Francisco Pereira. Distributed weight consolidation: A brain segmentation case study. In *proc of NIPS*, pages 4093–4103, 2018. 3

[25] H.B. McMahan, E. Moore, D. Ramage, S. Hampson, and B.A. Fast trust region for segmentation. In *Proc of ICAIS*, pages 1273–1282, 2017. 1

[26] H. Brendan McMahan, Eider Moore, Daniel Ramage, and Blaise Agüera y Arcas. Federated learning of deep networks using model averaging. *CoRR*, abs/1602.05629, 2016. 3

[27] Adriënne M Mendrik, Koen L Vincken, Hugo J Kuijf, Marcel Breeuwer, Willem H Bouvy, Jeroen De Bresser, Amir Alansary, Marleen De Bruijne, Aaron Carass, Ayman El-Baz, et al. MRBrainS challenge: online evaluation framework for brain image segmentation in 3T MRI scans. *Comp. Intel. and Neuro.*, 2015:1, 2015. 5

[28] Karthik Nandakumar, Nalini Ratha, Sharath Pankanti, and Shai Halevi. Towards deep neural network training on encrypted data. In *Proceedings of the IEEE Conference on Computer Vision and Pattern Recognition Workshops*, pages 0–0, 2019. 1

[29] Witold Oleszkiewicz, Peter Kairouz, Karol Piczak, Ram Rajagopal, and Tomasz Trzciński. Siamese generative adversarial privatizer for biometric data. In *proc of ACCV*, pages 482–497, 2018. 2, 3

[30] Pascal Paillier. Public-key cryptosystems based on composite degree residuosity classes. In *proc ICTACT*, pages 223–238, 1999. 2

[31] Francesco Pittaluga, Sanjeev Koppal, and Ayan Chakrabarti. Learning privacy preserving encodings through adversarial training. In *proc of IEEE WACV*, pages 791–799, 2019. 3

[32] Nisarg Raval, Ashwin Machanavajjhala, and Landon P Cox. Protecting visual secrets using adversarial nets. In *proc of CVPRW*, pages 1329–1332, 2017. 3

[33] Olaf Ronneberger, Philipp Fischer, and Thomas Brox. U-net: Convolutional networks for biomedical image segmentation. *CoRR*, abs/1505.04597, 2015. 1, 3, 4

[34] Bita Rouhani, Sadegh Riazi, and Farinaz Koushanfar. Deepsecure: Scalable provably-secure deep learning. In *in proc of Design Auto. Conf. (DAC)*, 2018. 1, 3

[35] Abhijit Guha Roy, Sailesh Conjeti, Nassir Navab, Christian Wachinger, Alzheimer’s Disease Neuroimaging Initiative, et al. QuickNAT: A fully convolutional network for quick and accurate segmentation of neuroanatomy. *NeuroImage*, 186:713–727, 2019. 5

[36] Proteek Chandan Roy and Vishnu Naresh Boddeti. Mitigating information leakage in image representations: A maximum entropy approach. *CoRR*, abs/1904.05514, 2019. 3

[37] Carole H. Sudre, Wenqi Li, Tom Vercauteren, Sébastien Ourselin, and M. Jorge Cardoso. Generalised dice overlap as a deep learning loss function for highly unbalanced segmentations. *CoRR*, abs/1707.03237, 2017. 4

[38] Praneeth Vepakomma, Tristan Swedish, Ramesh Raskar, Otkrist Gupta, and Abhimanyu Dubey. No peek: A survey of private distributed deep learning. *CoRR*, abs/1812.03288, 2018. 3

[39] Weiru Wang, Chi-Man Vong, Yilong Yang, and Pak-Kin Wong. Encrypted image classification based on multilayer extreme learning machine. *MSSP*, 28(3):851–865, 2017. 2

[40] Z. Wang, E. P. Simoncelli, and A. C. Bovik. Multiscale structural similarity for image quality assessment. In *proc of IEEE ACSSC*, pages 1398–1402, 2003. 5

[41] Zhenyu Wu, Zhangyang Wang, Zhaowen Wang, and Hailin Jin. Towards privacy-preserving visual recognition via adversarial training: A pilot study. In *proc of ECCV*, pages 606–624, 2018. 3

[42] Pengtao Xie, Misha Bilenko, Tom Finley, Ran Gilad-Bachrach, Kristin E. Lauter, and Michael Naehrig. Cryptonets: Neural networks over encrypted data. *CoRR*, abs/1412.6181, 2014. 3

[43] Chugui Xu, Ju Ren, Deyu Zhang, Yaoxue Zhang, Zhan Qin, and Kui Ren. GANobfuscator: Mitigating information leakage under gan via differential privacy. *IEEE TIFS*, 14(9):2358–2371, 2019. 3

[44] Qiang Yang, Yang Liu, Tianjian Chen, and Yongxin Tong. Federated machine learning: Concept and applications. *ACM Transactions on Intelligent Systems and Technology (TIST)*, 10(2):12, 2019. 3

[45] Tsung-Yen Yang, Christopher Brinton, Prateek Mittal, Mung Chiang, and Andrew Lan. Learning informative and private representations via generative adversarial networks. In *proc of ICBD*, pages 1534–1543, 2018. 3

[46] S.K. Zhou, H. Greenspan, and D. Shen. *Deep Learning for Medical Image Analysis*. Elsevier Science, 2017. 1

[47] M Tarek Ibn Ziad, Amr Alanwar, Moustafa Alzantot, and Mani Srivastava. Cryptoint: Privacy preserving processing over encrypted images. In *proc of IEEE CNS*, pages 570–575, 2016. 2